ACS NANO

www.acsnano.org

ARTICLE

Tuning the Ultrafast Response of Fano Resonances in Halide Perovskite Nanoparticles

Paolo Franceschini,* Luca Carletti,* Anatoly P. Pushkarev, Fabrizio Preda, Antonio Perri, Andrea Tognazzi, Andrea Ronchi, Gabriele Ferrini, Stefania Pagliara, Francesco Banfi, Dario Polli, Giulio Cerullo, Costantino De Angelis, Sergey V. Makarov, and Claudio Giannetti*

Cite This: *ACS Nano* 2020, 14, 13602–13610

Read Online

ACCESS | Metrics & More | Article Recommendations | Supporting Information

ABSTRACT: The full control of the fundamental photophysics of nanosystems at frequencies as high as few THz is key for tunable and ultrafast nanophotonic devices and metamaterials. Here we combine geometrical and ultrafast control of the optical properties of halide perovskite nanoparticles, which constitute a prominent platform for nanophotonics. The pulsed photoinjection of free carriers across the semiconducting gap leads to a subpicosecond modification of the far-field electromagnetic properties that is fully controlled by the geometry of the system. When the nanoparticle size is tuned so as to achieve the overlap between the narrowband excitons and the geometry-controlled Mie resonances, the ultrafast modulation of the transmittivity is completely reversed with respect to what is usually observed in nanoparticles with different sizes, in bulk systems, and in thin films. The interplay between chemical, geometrical, and ultrafast tuning offers an additional control parameter with impact on nanoantennas and ultrafast optical switches.

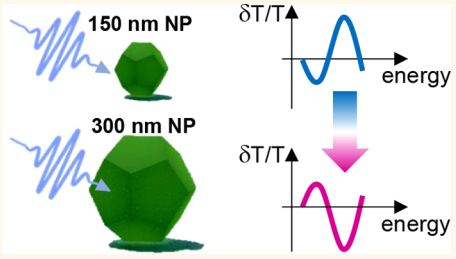

KEYWORDS: *Fano resonance, halide perovskites nanoparticles, ultrafast photophysics, nanophotonics, Mie resonances*

The study of light–matter interactions in halide perovskites (HPs) has revolutionized the photonics community in the past decade.[1,2] The wide interest in this class of materials, which comprises compounds of the form ABX_3, where A stands for organic (*e.g.*, CH_3NH_3=MA) or inorganic (*e.g.*, Cs) cations, B is usually lead (Pb), and X is chosen between the halogens I, Br, or Cl, mainly stems from their outstanding optoelectronic properties, such as strong excitonic resonances at room temperature,[3] tunable band-gaps, and emission wavelengths within the entire visible spectrum,[4−6] and long carrier diffusion lengths.[7,8] These features, combined with low-cost fabrication methods, boosted the development of photovoltaic solar cells with power conversion efficiency exceeding 20%.[9]

Halide perovskites constitute also a promising platform for ultrafast optical switching applications. Subpicosecond visible light pulses can be used to photoinject free carriers across the HP semiconducting gap, thus triggering the kind of multistep dynamics that is at the basis of any ultrafast photonic device operating at frequencies as high as several THz.[10−17] Tuning the density and energy-distribution of the photocarriers thus provides an additional control parameter for achieving the complete tunability of HPs optical properties on the picosecond time scale.

Recent advances in the development of HP-based metamaterials[18−21] and nanoantennas[22,23] brought into play an additional degree of freedom to control HP optical properties on ultrafast time scales.[24−26] In this framework, a geometry-based approach was proposed after the observation of tunable Fano resonances in nanoparticles (NPs), arising from the coupling of the discrete excitonic states to the continuum of the geometry-driven Mie modes of the nanostructures.[27] Tuning the interference by a suitable choice of the nanoparticle size allows one to dramatically modify the excitonic line shape, up to the point of reversing the scattering resonant peak into a dip.[27]

In this work, we combine geometrical and ultrafast manipulation of the optical conductivity of Mie-resonant

Received: July 9, 2020
Accepted: October 5, 2020
Published: October 15, 2020

https://dx.doi.org/10.1021/acsnano.0c05710
ACS Nano 2020, 14, 13602–13610

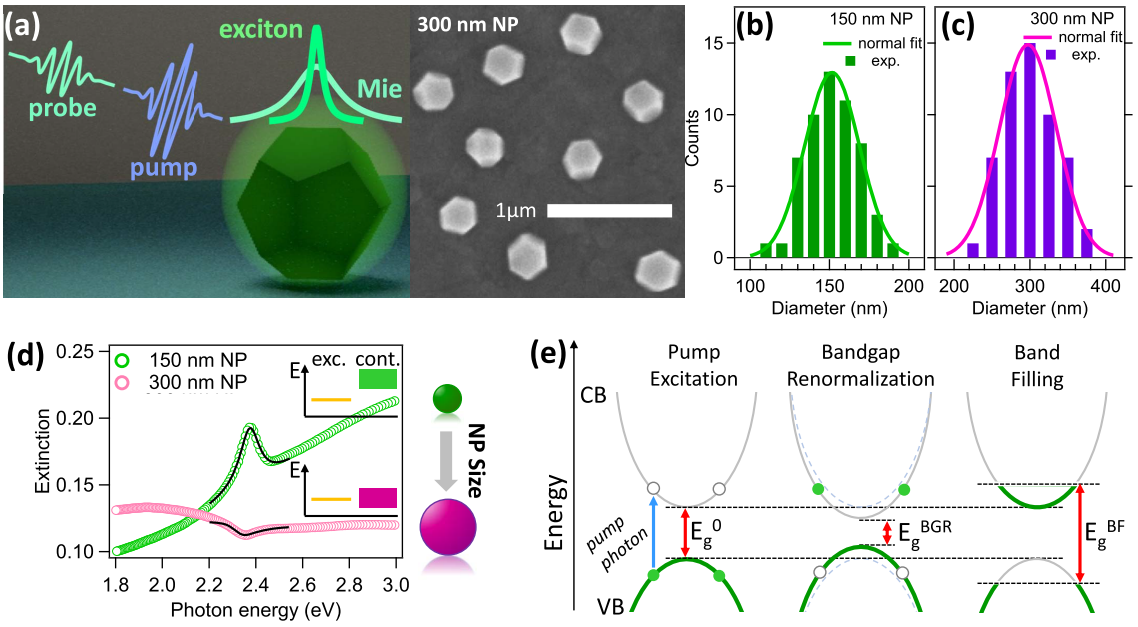

Figure 1. Structural and optical properties of hybrid perovskites nanoparticles. (a) Concept of the pump−probe experiment on HP nanoparticles. The right panel displays a scanning electron microscopy image of the 300 nm NPs sample. (b, c) Size distribution of $CsPbBr_3$ nanoparticles with average diameter $\bar{\phi}$ = 150 nm (b, green bars) and 300 nm (c, purple bars). The size distribution has been calculated by analysis of the scanning electron microscopy images. The solid line represents the normal fit to the experimental distributions. For both samples, the standard deviation of the normal distribution is 10% of the average size. (d) Experimental measured extinction spectra of the $CsPbBr_3$ nanoparticles with an average diameter of 150 nm (green markers) and 300 nm (pink markers). In the spectral region investigated in the time-resolved experiment, the extinction data have been fitted (solid black lines) with eq 1. For the 150 nm sample, we estimated q=(−18.1 ± 0.2) and Γ = (0.107 ± 0.003) eV, while q = (−0.41 ± 0.01) and Γ = (0.123 ± 0.005) eV for the 300 nm sample. The right panel sketches the energy overlap between the discrete excitonic level (yellow line) and the continuum of states (square), which gives rise to the Fano low-q resonance for 300 nm particles. (e) Schematics of the electron dynamics triggered by the pulsed photoexcitation (blue arrow): the initial creation of the nonthermal electron−hole distributions within the valence (VB) and conduction bands (CB) leads to the renormalization of the equilibrium gap, E_g^0, which reduces to $E_g = E_g^0 - \delta E_g^{BGR}$. At later times, the interactions drive the formation of a long-lived quasi-thermal distribution at the gap edges and a consequent increase of the effective optical band gap, $E_g = E_g^0 + \delta E_g^{BF}$.

$CsPbBr_3$ nanoparticles (see Figure 1a). Our time- and energy-resolved pump−probe data show that, when the nanoparticle size is tuned to achieve a dip in the excitonic Fano line shape, the photoinduced band gap renormalization and the subsequent band filling drive a modification of the optical constants, which is opposite as compared to that observed in bulk HP and in NPs exhibiting a peak in the excitonic Fano line shape. The analysis of the photophysics of Fano resonances in HP NPs is complemented by finite element simulations, which offer insights into the interplay between the nonequilibrium charge distribution and the coupling of the optical transitions to the geometry-controlled cavity modes and allow us to extract the intrinsic band-filling dynamics. The combination of optical and geometrical control offers an additional platform for ultrafast optoelectronic nanodevices and metamaterials. $CsPbBr_3$ nanoparticles, exhibiting tunable Fano resonances, represent a prospective building-block for ultrafast all-optical switching in nonlinear nanophotonic designs.[28,29] The observation of an opposite photoinduced response in nanoparticles exhibiting different Fano lineshapes represents an interesting method to control the nonlinear response of dielectric media in nanodevices and metamaterials with subwavelength spatial resolution.[30,31]

RESULTS

Isolated $CsPbBr_3$ nanoparticles with different average sizes (see distributions in Figure 1b,c) were deposited on a quartz transparent substrate with an average coverage density σ_{cov} = 3 NP/μm^2.[27] The samples were optically characterized by measuring the extinction, $X = -\log_{10} T$, where T is the sample transmission. In Figure 1d, we report the extinction, which includes both the scattering and absorption contributions, of samples with 150 and 300 nm average NP diameter ($\bar{\phi}$). In both cases, the extinction can be reproduced by the following expression:

$$X(\hbar\omega) = a \cdot \frac{\left[q \cdot \frac{\Gamma}{2} + \hbar\omega - (E_g - E_b)\right]^2}{\frac{\Gamma^2}{4} + [\hbar\omega - (E_g - E_b)]^2} + X_{bck}(\hbar\omega, E_g) \quad (1)$$

where the first term on the right-hand side represents a Fano asymmetric excitonic line width with amplitude a, centered at $E_g - E_b$, E_b being the exciton binding energy, and with a line shape controlled by the broadening parameter Γ and the profile index q. $X_{bck}(\hbar\omega, E_g)$ accounts for the absorption across the semiconducting edge at E_g (see section S2 for more details).

For 150 nm NPs, the small overlap between the excitonic line at $E_g - E_b \simeq 2.4$ eV and the Mie resonances results in a moderate asymmetry of the peak in the extinction spectrum (green markers in Figure 1d), corresponding to $q \simeq -18$ (high-q resonance). When the NP size is increased (300 nm), the overlap between the Mie modes and the excitonic resonance increases. As a result, the scattering contribution

https://dx.doi.org/10.1021/acsnano.0c05710
ACS Nano 2020, 14, 13602−13610

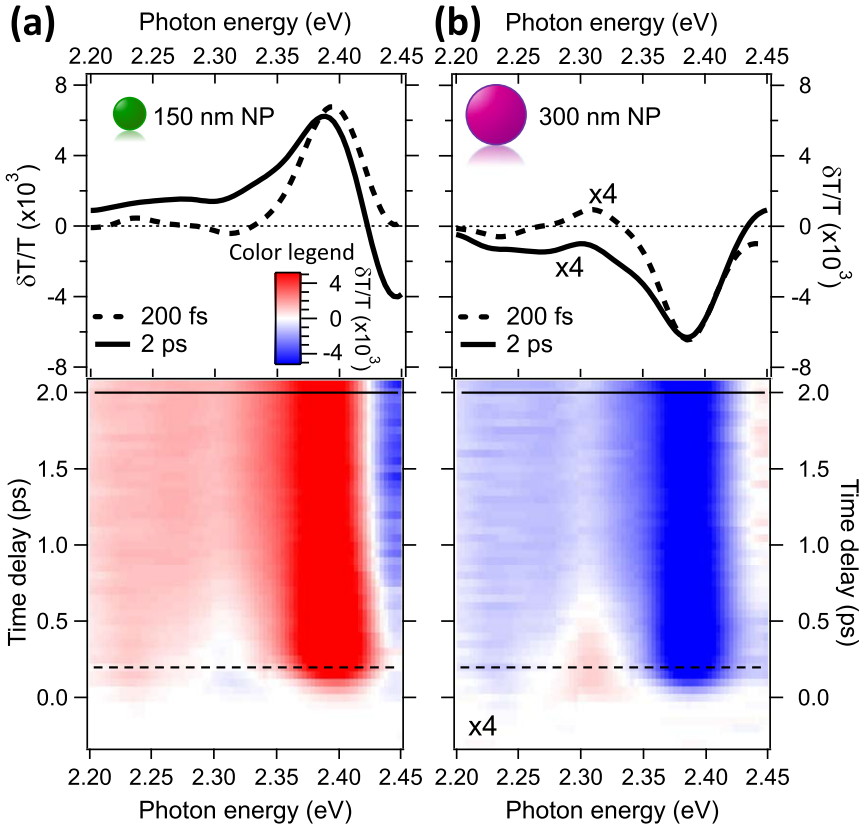

Figure 2. Ultrafast dynamics of the nanoparticle optical properties. Energy- and time-resolved differential transmission maps for 150 nm (a) and 300 nm (b) $CsPbBr_3$ nanoparticles pumped at 2.9 eV, with an incident fluence of 54 $\mu J/cm^2$. The top panels display $\delta T/T(\hbar\omega)$ spectra at fixed probe delays (200 fs, dashed line; 2 ps solid line) for 150 and 300 nm nanoparticles, respectively. For graphical reasons, the data reported in panel b are magnified by a factor of 4.

strongly increases,[27] thus turning the extinction line shape into a dip (pink markers in Figure 1d), which corresponds to $q \simeq -0.4$ (low-q resonance). The separate scattering and absorption contributions to the total extinction of single NPs are discussed in the Supporting Information.

In this work, we use ~40 fs (fwhm) light pulses at 2.9 eV photon energy to trigger the out-of-equilibrium dynamics in HP NPs. In general, it is known that in bulk semiconductors the sudden photogeneration of high-density nonthermal electrons (holes) within the conduction (valence) band (see Figure 1e) modifies the electron screening, thus shrinking the band gap. This phenomenon, known as band gap renormalization (BGR), manifests itself into a photoinduced absorption increase below the semiconducting band edge,[14] corresponding to a photoinduced dynamical decrease of the effective band gap, $E_g = E_g^0 - \delta E_g^{BGR}$. Within ≈1 ps, the electron−electron and electron−phonon interactions drive the relaxation of the nonthermal population and the creation of a long-lived quasi-thermal distribution, described by an effective temperature and chemical potential, which overfills the electron (hole) states at the band edges (see Figure 1e). The consequent bleaching of the band-edge transitions, known as band filling (BF) or dynamic Burstein−Moss effect,[33,34] leads to the photoinduced dynamical increase of the effective band gap, $E_g = E_g^0 + \delta E_g^{BF}$, until the equilibrium distribution is eventually recovered on the nanosecond time scale *via* interband recombination.[10] To address the role of the geometry in controlling the modulation of the optical properties consequent to the BGR and BF processes, we performed broadband pump−probe experiments on NPs all the way from Fano high-q to low-q resonance conditions. The pump-induced relative transmittivity variation, $\delta T/T(\hbar\omega, \Delta t)$, is measured in the 2.2−2.5 eV energy range by means of a delayed (Δt) supercontinuum white light probe detected through a collinear interferometer (GEMINI by NIREOS),[35,36] as described in the Methods. The energy- and time-dependent $\delta T/T(\hbar\omega, \Delta t)$ is reported for 150 and 300 nm NPs (see Figure 2a,b). More experimental data for different NP sizes are shown in Figure S1.

In the Fano high-q resonance condition (150 nm, Figure 2a), the $\delta T/T(\hbar\omega, \Delta t)$ signal is characterized by a short-lived negative component at $\hbar\omega \simeq 2.3$ eV and a long-lived signal, which turns from positive to negative at the exciton peak at $E_g - E_b \simeq 2.4$ eV. The presence of two different spectral components can be appreciated by plotting $\delta T/T$ spectra at different delays (Δt = 0.2 and 2 ps, top panel of Figure 2a). The negative transmittivity variation at short delays reflects a photoinduced increase of below-gap absorption, which is the signature of the BGR effect, as already observed in thin films.[14] On the picosecond time scale, this effect decays as a result of hot carrier cooling through electron−phonon interactions.[14] As a consequence, after ~2 ps the positive (negative) transmittivity variation at $\hbar\omega < (>)2.4$ eV can be reproduced, over the entire frequency range, by a rigid blue-shift, by $\delta E_g = (5.1 \pm 0.4)$ meV, of the excitonic line in eq 1. Such a shift is the typical manifestation of the conventional band filling effect, which has been already reported in HP thin-films.[10] We remark that the transmittivity variation measured in our pump−probe

https://dx.doi.org/10.1021/acsnano.0c05710
ACS Nano 2020, 14, 13602−13610

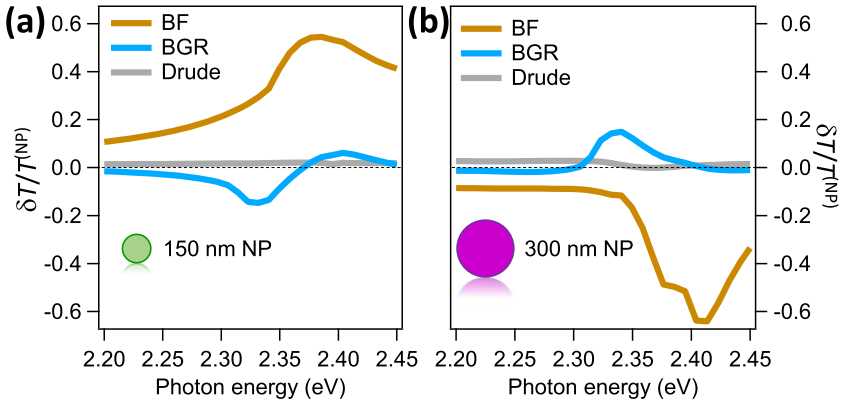

Figure 3. Numerical simulations. Differential transmittivity spectrum, $\delta T/T^{(NP)}(\hbar\omega)$, calculated for individual (a) 150 nm and (b) 300 nm nanoparticles. The separate contributions of the bandgap renormalization (BGR), band filling (BF), and Drude effects to the total signal are calculated by assuming the photoinjected free carrier density $n_{fc} \simeq 1.2 \times 10^{20}$ cm^{-3}, for both nanoparticle sizes.

experiment refers to the effective response of the sample, which can be modeled as an inhomogeneous film with $CsPbBr_3$ NPs, with volume filling fraction f_{vol}. Therefore, in order to quantitatively compare our results to previous data on thin films, we extracted the pump-induced shift of the band gap of the individual nanoparticles (δE_g^{NP}) by calculating the scaling factor ($\tilde{C}$), which relates δE_g^{NP} to the measured effective δE_g. As described in section S2, we adopted the Modified Maxwell–Garnett Mie (MMGM) theory[37] for the effective medium, which accounts for size-dispersed spherical particles embedded in a host matrix, to calculate the scaling factor as the ratio between the intrinsic absorption variation of an individual NP and the effective absorption variation of the film. From our analysis, we estimated $\tilde{C} = 60 \pm 40$. Considering that, for small shifts, the transmittivity variation in the proximity of a peak is directly proportional to the shift amplitude, we can thus assume that $\delta E_g^{NP} \simeq \tilde{C} \cdot \delta E_g = (300 \pm 200)$ meV, which is in quantitative agreement with data reported in ref 10.

The nonequilibrium optical response of $CsPbBr_3$ nanoparticles progressively changes when the NP size is increased and the overlap between the exciton resonance at ~2.4 eV and the geometry-controlled continuum of the Mie modes is enhanced. In the Fano low-q resonance condition, obtained for 300 nm NP size, the $\delta T/T(\hbar\omega, \Delta t)$ signals associated with both the band gap renormalization and band filling effects are reversed, as shown in Figure 2b. In this condition, the subpicosecond below-gap transmittivity change is positive, thus suggesting a photoinduced decrease of below-gap absorption in opposition to the conventional band gap renormalization effect measured in films and nanoparticles far from the Fano low-q resonance condition.

Our results demonstrate that the nonequilibrium optical properties of $CsPbBr_3$ NPs following ultrafast excitation are crucially controlled by the NP size. The photogenerated electron/hole population in the conduction and valence bands gives rise to a photoinduced variation of the far-field optical properties, which qualitatively and quantitatively depend on the interference between the excitonic resonance and the geometrically controlled Mie modes. To gain further insights into the interplay between nonequilibrium photoinjected free carriers and the geometry-controlled Fano interference, we performed full-vectorial numerical electromagnetic simulations implemented with the finite element method in COMSOL. In these numerical calculations, we considered isolated HP nanospheres deposited on a quartz substrate with refractive index 1.45. The numerical simulations of the full electromagnetic problem go beyond the Mie theory for isolated NPs, which is presented in section S6, and allow us to account for the NP–substrate interaction that affects spectral position, amplitude, and phase of the resonances in the NP.[38]

The frequency dependent transmittivity variation of the single NP is calculated as $\delta T/T^{(NP)}(\hbar\omega) = 10^{-(X_{out}^{NP}(\hbar\omega) - X_{eq}^{NP}(\hbar\omega))} - 1$ (for details, see Methods). The equilibrium extinction, $X_{eq}^{NP}(\hbar\omega)$, is obtained by solving the NP scattering problem and assuming the complex refractive index of bulk $CsPbBr_3$ (extracted from ref 27). The out-of-equilibrium extinction, $X_{out}^{NP}(\hbar\omega)$, is obtained by properly modifying the equilibrium optical properties to account for the effect of photogenerated nonequilibrium carriers. More specifically, we assume that the photoexcitation process initially injects an excess density of electrons (n_e) and holes (n_h) approximately equal to the density of absorbed photons, *i.e.*, $n_e \simeq n_h \simeq n_{ph}$. On the subpicosecond time scale, the photoinjected free carrier density, $n_{fc} = n_e + n_h \simeq 2n_{ph} \simeq 1.2 \times 10^{20}$ cm^{-3} (see the Methods for the calculation of n_{ph}), overcomes the screening critical concentration, $n_{cr} \approx 3.4 \times 10^{18}$ cm^{-3} (see section S5 of the Supporting Information),[32] thus leading to a photoinduced bandgap renormalization and a related change of the absorption coefficient expressed as[32]

$$\delta\alpha_{BGR}(\hbar\omega; n_{fc}/n_{cr}) = \alpha_{eq}(\hbar\omega; E_g^0 - \delta E_{BGR}(n_{fc}/n_{cr})) - \alpha_{eq}(\hbar\omega; E_g^0) \quad (2)$$

Within ≈1 ps, the carrier–carrier and carrier–phonon interactions lead to the relaxation of the photoinjected free carriers and to the onset of a quasi-thermal effective carriers distribution which completely fills the states at the bottom (top) of the conduction (valence) band. The bleaching of the gap-edge transitions (band filling) manifests itself as[32]

$$\delta\alpha_{BF}(\hbar\omega; n_{fc}, T^*) = \alpha_{eq}(\hbar\omega; E_g^0)[f_v(\hbar\omega; E_{F_v}^*, T^*) - f_c(\hbar\omega; E_{F_c}^*, T^*) - 1] \quad (3)$$

where the effective Fermi–Dirac populations in the valence and conduction bands, f_v and f_c, respectively, are controlled by the effective Fermi levels $E_{F_v}^*$ and $E_{F_c}^*$ and by the effective temperature T^*. The photoinduced absorption change related

https://dx.doi.org/10.1021/acsnano.0c05710
ACS Nano 2020, 14, 13602–13610

to transition of free carriers within the conduction (valence) band is accounted for by a Drude model, as described in section S5 of the Supporting Information. We calculated $\delta T/T^{(NP)}(\hbar\omega)$ for different NP sizes, namely, 150 and 300 nm (Figure 3a,b, respectively), corresponding to the Fano high-q resonance and low-q resonance conditions. While the Drude contribution is always negligible (see Figure 3), the BGR and BF dominate the transmittivity change, as can be evidenced by calculating separately the two contributions to the $\delta T/T^{(NP)}(\hbar\omega)$ signal. For both NP sizes, the BGR effect has been estimated by assuming $n_{fc}/n_{cr} \simeq 2n_{ph}/n_{cr} = 35$ in eq 2. The BF effect has been reproduced by assuming that the effective thermal energy of the free carriers is given by the excess energy injected by the pump photons and equally shared between electrons and holes, *i.e.*, $3/2kT^* = (\hbar\omega_p - E_g^0)/2$. Considering $\hbar\omega_p = 2.9$ eV and $E_g^0 \simeq 2.4$ eV, we obtain $T^* \simeq 3000$ K. $E_{F_v}^*$ and $E_{F_c}^*$ are then self-consistently calculated (see eqs S21 and S22) assuming $n_{fc} = 2n_{ph}$. The results reported in Figure 3 show that, for 150 nm NP size, the BGR results in an additional below edge absorption (negative $\delta T/T$), which is opposite to the signal related to the BF process. In contrast, when the NP size matches the Fano low-q resonance condition (300 nm, Figure 3b), both the BGR and BF contributions to the differential transmittivity variation are of opposite sign as compared to the high-q resonant case. Moreover, the results obtained from the simulations are consistent with the experimental data obtained for a wider set of $CsPbBr_3$ NP samples. Indeed, in the case of nanoparticles with average sizes of ~100 nm and ~220 nm, whose extinction spectrum is characterized by a peak (high-q) near the exciton line (see Figure S1a), their out-of-equilibrium optical properties (reported in Figure S1b,d) exhibit spectral features similar to those reported for 150 nm NP sample. These numerical results support our experimental findings and demonstrate that the photoinduced modulation of the NP optical properties is controlled by the geometry of the system.

The numerical results reported in Figure 3 offer important insights into the photophysics of HP NPs and provide a guide for disentangling the BGR and BF dynamics, which experimentally overlap on the picosecond time scale. The results reported in Figure 3a,b indicate that, for both NP sizes, the $\delta T/T^{(NP)}$ at $\hbar\omega \simeq 2.2$ eV is dominated by the BF effect, whereas the BGR signal is negligible. As a consequence, time traces at this photon energy, although smaller in amplitude with respect to data at higher photon energy, directly reproduce the dynamics of the BF alone. In Figure 4a,b, we report $\delta T/T(\hbar\omega = 2.23$ eV, $\Delta t)$ time traces (black dots), which can be fitted by a single exponential function (black lines) with similar time constant $\tau_{BF} = 480 \pm 20$ fs. The BGR dynamics can then be retrieved by analyzing the time-traces taken at different photon energies for which the BGR contribution is not negligible. In Figure 4a,b, we report $\delta T/T(\hbar\omega = 2.3$ eV, $\Delta t)$ time traces (red dots), which exhibit a multiexponential behavior. In Figure 4c, we report the components of the multiexponential fit which directly represent the time evolution of the actual BGR process; the curves are obtained by subtracting the properly scaled BF contribution from the full $\delta T/T$ dynamics at $\hbar\omega = 2.3$ eV (see section S4 for more details). For both NP sizes, the build-up time of the BGR signal is ≈200 fs, whereas the relaxation of the nonthermal carriers responsible for the BGR takes place within 400 ± 10 fs, a time scale compatible with the carrier cooling

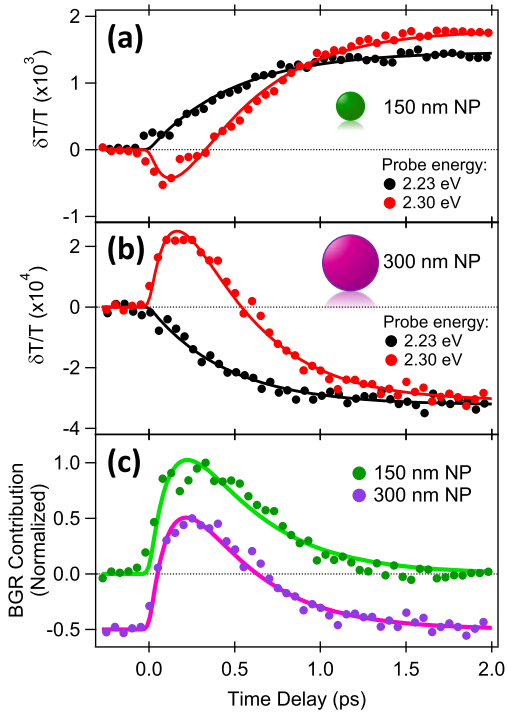

Figure 4. Disentangling band filling and bandgap renormalization. Differential time traces at specific photon energies are reported for NP sizes matching the Fano high-q resonance (150 nm, panel a) and low-q resonance conditions (300 nm, panel b). The black solid lines represent the single exponential fitting to the time traces taken at $\hbar\omega = 2.23$ eV (black dots). The red solid lines represent the multiexponential fitting to the time traces taken at $\hbar\omega = 2.3$ eV (red dots). Panel c displays the BGR signal obtained by subtracting the BF dynamics from the time traces taken at $\hbar\omega = 2.3$ eV and shown in panels a and b. The solid lines represent the exponential fitting to the BGR dynamics.

mediated by the coupling to optical phonons.[39] We underline that, in the time-resolved traces, the dynamics of the $\delta T/T$ signal is proportional to the nonequilibrium population within the valence and conduction bands. This population, which is bottlenecked by the presence of the gap, decays on a time scale much longer than the inverse of the exciton line width ($\sim\hbar/\Gamma$ = 6 fs) that accounts for the whole of quasi-elastic scattering processes which reduce the exciton lifetime. The procedure here introduced and based on time- and frequency-resolved optical measurements constitutes a way to disentangle the BGR and BF processes. Our results show that, microscopically, the two processes are almost independent of the NP size, as expected since the exciton Bohr's radius (~7 nm)[5] is much smaller than the NP size. The observed inversion of the $\delta T/T(\hbar\omega, \Delta t)$ signals in the Fano low-q resonance condition is thus a genuine effect of the geometry of the system, which controls the subpicosecond modulation of the optical properties.

The numerical simulations also reproduce the local electric field enhancement *FE*, defined as the ratio between the modulus of the electric field $(\vec{E}(x,y,z))$ and the amplitude of the incident plane wave (E_0): $FE = \|\vec{E}(x,y,z)\|/E_0$. Figure 5 shows equilibrium and out-of-equilibrium *FE* at 2.38 eV for a single nanoparticle with 150 and 300 nm diameter sizes. The black arrows represent the electric field vector for the same excitation parameters used to obtain the plots reported in Figure 3. For 150 nm NPs, the equilibrium resonance (panel a)

https://dx.doi.org/10.1021/acsnano.0c05710
ACS Nano 2020, 14, 13602−13610

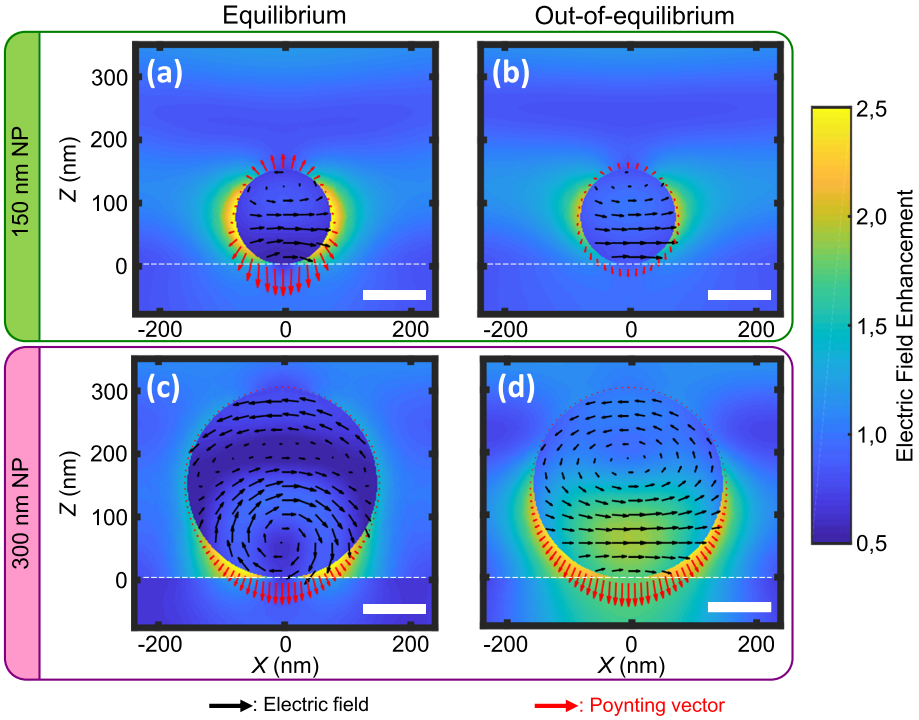

Figure 5. Electric field enhancement. Electric field enhancement on the plane of the vertical cross-section of the nanoparticle. The panels show the equilibrium (a, c) and out-of-equilibrium (b, d) *FE* for a single $CsPbBr_3$ NP with diameters of 150 (a, b) and 300 nm (c, d). The incident monochromatic wave centered at 2.38 eV propagates from the top to the bottom along the *Z* axis. The black arrows represent the electric field vector $\vec{E}$ in the NP volume. The red arrows represent the Poynting vector *S* outside the NP surface. The dashed white line represents the substrate surface. The scale bar is 100 nm.

is dominated by the electric dipole (ED) mode. The ED spatial pattern is maintained also in out-of-equilibrium conditions (panel b). On the other hand, the nature of the resonance dramatically changes for 300 nm NPs. The electric field distribution in Figure 5c suggests that both ED and MD (magnetic dipole) resonances contribute to the electromagnetic response at equilibrium, the latter exhibiting a typical field leakage toward the substrate. The MD contribution in 300 nm NPs, for the probe spectral region considered (2.20−2.45 eV), is consistent with the observation[40] that the MD mode takes place when the relation $\lambda_0/n \approx \bar{\phi}$ is fulfilled, with λ_0/n being the light wavelength inside the particle. Indeed, from ref 27, $n = 2.1$ at $\hbar\omega = 2.2$ eV, which gives $\lambda_0/n = 270 \approx 300$ nm (see multipole modes decomposition for NPs of different sizes in section S6). In the Fano low-*q* resonance condition, the photoexcitation strongly alters the mode spatial distribution (panel d) by shifting up the MD center of mass and increasing the ED mode contribution at the NP−substrate interface.

In order to connect the near field solutions to the total scattering, it is instructive to plot the Poynting vector at the NP interface (red arrows). In the Fano high-*q* resonance condition (150 nm NPs in panels a and b), photoexcitation leads to a quenching of the total scattered energy, corresponding to the positive transmittivity variation measured in the experiments. In contrast, the out-of-equilibrium Poynting vector in Fano low-*q* resonance NPs (300 nm NPs in panels c and d) indicates an overall transient scattering enhancement associated with the ED and MD photoinduced change and corresponding to the negative measured transmittivity variation.

CONCLUSIONS

In conclusion, we have studied the photoinduced subpicosecond optical modulation of the Fano resonance formed by the coupling of an excitonic state with Mie modes in halide perovskite NPs. In particular, we have demonstrated that the ultrafast modification of the optical properties induced by the band gap renormalization and band filling mechanisms dramatically depends on the geometry of the NPs. In the low-*q* resonance Fano condition, the contribution of the two effects to the relative transmittivity variation is completely reversed with respect to the high-*q* resonant case and to what was previously observed in thin films and bulk materials.[16] Importantly, this is the demonstration of the ultrafast control of the optical response in nanoparticles where Mie resonances are coupled with excitons. In previous studies, the ultrafast all-optical switching in Mie-resonant nanoparticles was carried out with standard semiconductors like amorphous silicon[28,41−43] and gallium arsenide,[44] for which excitonic effects are negligible at room temperature. Beside the physical effects arising from the coupling between the exciton and Mie modes, there is an important advantage of high absorption and sharp band-edge in $CsPbBr_3$ perovskites, allowing us to greatly reduce the fluence required to observe ultrafast tuning. $CsPbBr_3$ nanoparticles exhibit an amplitude of the transmittivity modulation that is 2 orders of magnitude larger as compared to that measured in silicon-based Mie resonators under similar photoexcitation conditions.[42] Although in this work we focused on $CsPbBr_3$ nanoparticles, the results and modeling discussed simply rely on the geometry-driven overlap between the exciton line and the continuum of Mie resonances. As a consequence, the present results can be promptly extended to a wider class of perovskite-based

https://dx.doi.org/10.1021/acsnano.0c05710
ACS Nano 2020, 14, 13602−13610

nanonstructures. The present results offer insights into the photophysics of halide perovskite nanoparticles and provide an additional parameter to control their optical properties at frequencies as high as few terahertz, with impact on perovskite-based optoelectronic devices, metamaterials, and switchable nanoantennas.

METHODS

Samples. Perovskite NPs are deposited on the ITO and glass substrates according to the following protocol. A solution **1** consists of lead(II) bromide ($PbBr_2$, 36.7 mg, 0.1 mmol) and cesium(I) bromide (CsBr, 21.2 mg, 0.1 mmol) dissolved in 1 mL of anhydrous dimethyl sulfoxide (DMSO). A solution **2** consists of poly(ethylene oxide) (PEO, average Mw 70 000, 10 mg) stirred at 300 rpm in 1 mL of DMSO at 70° for 10 h. **1** and **2** are mixed in a 1:3 mass ratio and stirred at 100° for 10 min to give a perovskite-polymer ink. The latter is deposited on precleaned glass and ITO substrates by spin-casting at 1500 rpm for 1 min. The deposited films are annealed at 130° for 3 min to produce NPs with an average size of 150 nm and at 80° for 10 min to obtain NPs with an average size of 300 nm. All the procedures are conducted inside a N_2-filled glovebox with both O_2 and H_2O levels not exceeding 1 ppm. Extinction spectra are measured in a UV−vis-NIR spectrophotometer (Shimadzu UV-2600).

Time-Resolved Pump−Probe Spectroscopy. The optical pump−probe setup is based on a Yb-laser system (Pharos, Light Conversion), which delivers 37.5 μJ, 270 fs pulses at 1030 nm central wavelength, and 400 kHz repetition rate. A portion of the laser with 30 μJ energy is used to pump an optical parametric amplifier (Orpheus-F, Light Conversion). The output signal at 850 nm is frequency doubled to obtain a pump pulse at 425 nm (2.9 eV), bandwidth[45] $\Delta\lambda \sim 7$ nm, with 52 nJ energy per pulse that is focused within 350 μm spot size (fwhm). The 54 $\mu J/cm^2$ incident pump fluence is such that the average absorbed photon density is $n_{ph} \simeq 6 \times 10^{19}$ cm^{-3} (see section S3 for more details). The other portion of the laser is focused on a sapphire crystal to generate a white-light continuum probe ranging from 500 to 1000 nm, which is then reduced to the region 500−600 nm (2.1−2.5 eV) by a colored bandpass glass filter (~1 mW). The pump is modulated by a mechanical chopper working at 2.5 kHz. The pump pulse is delayed in time with respect to the probe pulse by using a linear motorized stage (Physik Instrumente M403.2DG). The pump and the probe beams are orthogonally polarized: the pump is linearly horizontally polarized, whereas the probe is vertically polarized. The two beams are noncollinearly focused onto the sample: the pump impinges on the sample at normal incidence, while the incident angle of the probe is less than 10°. After the interaction with the sample, the linear and differential transmission spectra (at fixed pump−probe delay) are detected by means of a common-path birefringent interferometer, GEMINI (from NIREOS), which generates two collinear replicas of the incoming light. When the relative delay between the two probe replicas is varied, the light interferogram is obtained on a single-pixel photodiode. The linear transmission spectrum is obtained by computing the Fourier transform of the interferogram, while the differential transmission spectrum is retrieved by computing the Fourier transform of the interferogram demodulated by a lock-in amplifier at the chopping frequency. The pump-induced relative transmittivity variation is defined as $\delta T/T(\hbar\omega, \Delta t) = [T_{out}(\hbar\omega, \Delta t) - T_{eq}(\hbar\omega)]/T_{eq}(\hbar\omega)$, where T_{out} and T_{eq} are the out-of- and equilibrium transmittivities.

Simulations. We performed full-vectorial numerical simulations implemented with the finite element method in COMSOL. In our simulations, we consider the linear scattering problem of an electric field impinging on isolated $CsPbBr_3$ nanospheres deposited on a quartz substrate. From the simulations, we calculated the absorption and scattering cross-section of the single nanoparticle, C_{abs} and C_{sca}, respectively, to obtain the extinction cross-section C_{ext} of the single nanoparticle as $C_{ext} = C_{abs} + C_{sca}$.[46] The absorption (scattering) cross-section is calculated as $C_{abs} = w_{abs}/I_i$ ($C_{sca} = w_{sca}/I_i$), where w_{abs} (w_{sca}) is the rate at which the energy is absorbed (scattered) by the particle and I_i is the incident light intensity.[46] The incident field is a linearly polarized plane wave since the focal spot size in the experiment is much larger than the sphere diameter. To obtain the transmittivity of the layer from C_{ext}, we assumed that the nanoparticles are weakly coupled and that they are uniformly distributed on the substrate surface with a coverage distribution density $\sigma_{cov} = 3$ NP/μm^2. The transmittivity is given by $T = 10^{-X}$, where the extinction X is related to C_{ext} through $X = \sigma_{cov} \cdot C_{ext} \cdot \log_{10} e$.[46] The equilibrium transmittivity of the nanoparticle is obtained by solving the linear scattering problem for a single $CsPbBr_3$ sphere, where the equilibrium complex refractive index equals the experimental refractive index of $CsPbBr_3$ thin films, reported in ref 27. The out-of-equilibrium transmittivity is obtained by solving the linear scattering problem for a single $CsPbBr_3$ sphere, where the equilibrium complex refractive index is modified according to eqs 2 and 3. This procedure is applied to nanoparticles with diameters of 150 and 300 nm.

ASSOCIATED CONTENT

Supporting Information

The Supporting Information is available free of charge at https://pubs.acs.org/doi/10.1021/acsnano.0c05710.

Equilibrium extinction spectra for additional samples, time- and energy-resolved differential transmission maps for additional samples, details on the effective medium optical properties analysis, calculation of the pump photon density, details on the analysis of the time-resolved traces, models of the dynamics of the single nanoparticle optical properties, efficiency factors, and mode decompositions of the single particle

AUTHOR INFORMATION

Corresponding Authors

Paolo Franceschini − *Department of Mathematics and Physics and ILAMP (Interdisciplinary Laboratories for Advanced Materials Physics), Università Cattolica del Sacro Cuore, Brescia I-25121, Italy; Department of Physics and Astronomy, KU Leuven, 3001 Leuven, Belgium*;
Email: paolo.franceschini@unicatt.it

Luca Carletti − *Department of Information Engineering, University of Padova, Padova 35131, Italy; Department of Information Engineering, University of Brescia, Brescia 25123, Italy*; orcid.org/0000-0001-6268-9817;
Email: luca.carletti@unibs.it

Claudio Giannetti − *Department of Mathematics and Physics and ILAMP (Interdisciplinary Laboratories for Advanced Materials Physics), Università Cattolica del Sacro Cuore, Brescia I-25121, Italy*; orcid.org/0000-0003-2664-9492;
Email: claudio.giannetti@unicatt.it

Authors

Anatoly P. Pushkarev − *ITMO University, Saint Petersburg 197101, Russia*; orcid.org/0000-0002-1793-6812

Fabrizio Preda − *Dipartimento di Fisica, Politecnico di Milano, Milano 20133, Italy; NIREOS S.R.L., 20158 Milano, Italy*, www.nireos.com

Antonio Perri − *Dipartimento di Fisica, Politecnico di Milano, Milano 20133, Italy; NIREOS S.R.L., 20158 Milano, Italy*, www.nireos.com

Andrea Tognazzi − *Department of Information Engineering, University of Brescia, Brescia 25123, Italy; National Institute of Optics (INO), Consiglio Nazionale delle Ricerche (CNR), Brescia 25123, Italy*

Andrea Ronchi − *Department of Mathematics and Physics and ILAMP (Interdisciplinary Laboratories for Advanced Materials*

https://dx.doi.org/10.1021/acsnano.0c05710
ACS Nano 2020, 14, 13602−13610

Physics), Università Cattolica del Sacro Cuore, Brescia I-25121, Italy; Department of Physics and Astronomy, KU Leuven, 3001 Leuven, Belgium

Gabriele Ferrini − *Department of Mathematics and Physics and ILAMP (Interdisciplinary Laboratories for Advanced Materials Physics), Università Cattolica del Sacro Cuore, Brescia I-25121, Italy*

Stefania Pagliara − *Department of Mathematics and Physics and ILAMP (Interdisciplinary Laboratories for Advanced Materials Physics), Università Cattolica del Sacro Cuore, Brescia I-25121, Italy*

Francesco Banfi − *FemtoNanoOptics Group, Université de Lyon, CNRS, Université Claude Bernard Lyon 1, Institut Lumière Matière, F-69622 Villeurbanne, France;* orcid.org/0000-0002-7465-8417

Dario Polli − *Dipartimento di Fisica, Politecnico di Milano, Milano 20133, Italy; NIREOS S.R.L., 20158 Milano, Italy,* www.nireos.com; orcid.org/0000-0002-6960-5708

Giulio Cerullo − *Dipartimento di Fisica, Politecnico di Milano, Milano 20133, Italy;* orcid.org/0000-0002-9534-2702

Costantino De Angelis − *Department of Information Engineering, University of Brescia, Brescia 25123, Italy; National Institute of Optics (INO), Consiglio Nazionale delle Ricerche (CNR), Brescia 25123, Italy;* orcid.org/0000-0001-8029-179X

Sergey V. Makarov − *ITMO University, Saint Petersburg 197101, Russia;* orcid.org/0000-0002-9257-6183

Complete contact information is available at: https://pubs.acs.org/10.1021/acsnano.0c05710

Notes

The authors declare no competing financial interest.

ACKNOWLEDGMENTS

P.F. and C.G acknowledge financial support from MIUR through PRIN 2015 (Prot. 2015C5SEJJ001) and PRIN 2017 (Prot. 20172H2SC4) Programs. G.F., S.P., and C.G. acknowledge support from Università Cattolica del Sacro Cuore through Grants D.1, D.2.2, and D.3.1. L.C. acknowledges STARS StG project PULSAR. S.M and A.P. acknowledge the Russian Science Foundation (project 20-73-10183). F.B. acknowledges financial support from the IDEXLYON Project-Programme Investissements d'Avenir (Grant ANR-16-IDEX-0005), France. NIREOS acknowledges financial support from the European Union's Horizon 2020 Research and Innovation Programme under Grant Agreement No. 814492 (SimDOME).

REFERENCES

(1) A Decade of Perovskite Photovoltaics. *Nat. Energy* **2019**, *4*, 1.

(2) Fu, Y.; Zhu, H.; Chen, J.; Hautzinger, M. P.; Zhu, X.-Y.; Jin, S. Metal Halide Perovskite Nanostructures for Optoelectronic Applications and the Study of Physical Properties. *Nat. Rev. Mater.* **2019**, *4*, 169−188.

(3) Green, M. A.; Ho-Baillie, A.; Snaith, H. J. The Emergence of Perovskite Solar Cells. *Nat. Photonics* **2014**, *8*, 506−514.

(4) Jang, D. M.; Park, K.; Kim, D. H.; Park, J.; Shojaei, F.; Kang, H. S.; Ahn, J.-P.; Lee, J. W.; Song, J. K. Reversible Halide Exchange Reaction of Organometal Trihalide Perovskite Colloidal Nanocrystals for Full-Range Band Gap Tuning. *Nano Lett.* **2015**, *15*, 5191−5199.

(5) Protesescu, L.; Yakunin, S.; Bodnarchuk, M. I.; Krieg, F.; Caputo, R.; Hendon, C. H.; Yang, R. X.; Walsh, A.; Kovalenko, M. V. Nanocrystals of Cesium Lead Halide Perovskites ($CsPbX_3$, X = Cl, Br and I): Novel Optoelectronic Materials Showing Bright Emission with Wide Color Gamut. *Nano Lett.* **2015**, *15*, 3692−3696.

(6) Byun, H. R.; Park, D. Y.; Oh, H. M.; Namkoong, G.; Jeong, M. S. Light Soaking Phenomena in Organic - Inorganic Mixed Halide Perovskite Single Crystals. *ACS Photonics* **2017**, *4*, 2813−2820.

(7) Wehrenfennig, C.; Eperon, G. E.; Johnston, M. B.; Snaith, H. J.; Herz, L. M. High Charge Carrier Mobilities and Lifetimes in Organolead Trihalide Perovskites. *Adv. Mater.* **2014**, *26*, 1584−1589.

(8) Dong, Q.; Fang, Y.; Shao, Y.; Mulligan, P.; Qiu, J.; Cao, L.; Huang, J. Electron-Hole Diffusion Lengths > 175 μm in Solution-Grown $CH_3NH_3PbI_3$ Single Crystals. *Science* **2015**, *347*, 967−970.

(9) Yang, W. S.; Noh, J. H.; Jeon, N. J.; Kim, Y. C.; Ryu, S.; Seo, J.; Seok, S. I. High-Performance Photovoltaic Perovskite Layers Fabricated through Intramolecular Exchange. *Science* **2015**, *348*, 1234−1237.

(10) Manser, J. S.; Kamat, P. V. Band Filling with Free Charge Carriers in Organometal Halide Perovskites. *Nat. Photonics* **2014**, *8*, 737.

(11) Sheng, C.; Zhang, C.; Zhai, Y.; Mielczarek, K.; Wang, W.; Ma, W.; Zakhidov, A.; Vardeny, Z. V. Exciton *versus* Free Carrier Photogeneration in Organometal Trihalide Perovskites Probed by Broadband Ultrafast Polarization Memory Dynamics. *Phys. Rev. Lett.* **2015**, *114*, 116601.

(12) Milot, R. L.; Eperon, G. E.; Snaith, H. J.; Johnston, M. B.; Herz, L. M. Temperature-Dependent Charge-Carrier Dynamics in $CH_3NH_3PbI_3$ Perovskite Thin Films. *Adv. Funct. Mater.* **2015**, *25*, 6218−6227.

(13) Yang, Y.; Ostrowski, D. P.; France, R. M.; Zhu, K.; van de Lagemaat, J.; Luther, J. M.; Beard, M. C. Observation of a Hot-Phonon Bottleneck in Lead-Iodide Perovskites. *Nat. Photonics* **2016**, *10*, 53−59.

(14) Price, M. B.; Butkus, J.; Jellicoe, T. C.; Sadhanala, A.; Briane, A.; Halpert, J. E.; Broch, K.; Hodgkiss, J. M.; Friend, R. H.; Deschler, F. Hot-Carrier Cooling and Photoinduced Refractive Index Changes in Organic-Inorganic Lead Halide. *Nat. Commun.* **2015**, *6*, 8420.

(15) Herz, L. M. Charge-Carrier Dynamics in Organic - Inorganic Metal Halide Perovskites. *Annu. Rev. Phys. Chem.* **2016**, *67*, 65−89.

(16) Tamming, R. R.; Butkus, J.; Price, M. B.; Vashishtha, P.; Prasad, S. K. K.; Halpert, J. E.; Chen, K.; Hodgkiss, J. M. Ultrafast Spectrally Resolved Photoinduced Complex Refractive Index Changes in $CsPbX_3$ Perovskites. *ACS Photonics* **2019**, *6*, 345−350.

(17) Palmieri, T.; Baldini, E.; Steinhoff, A.; Akrap, A.; Kollár, M.; Horváth, E.; Forró, L.; Jahnke, F.; Chergui, M. Mahan Excitons in Room-Temperature Methylammonium Lead Bromide Perovskites. *Nat. Commun.* **2020**, *11*, 850.

(18) Gholipour, B.; Adamo, G.; Cortecchia, D.; Krishnamoorthy, H. N. S.; Birowosuto, M. D.; Zheludev, N. I.; Soci, C. Organometallic Perovskite Metasurfaces. *Adv. Mater.* **2017**, *29*, 1604268.

(19) Makarov, S. V.; Milichko, V.; Ushakova, E. V.; Omelyanovich, M.; Cerdan Pasaran, A.; Haroldson, R.; Balachandran, B.; Wang, H.; Hu, W.; Kivshar, Y. S.; Zakhidov, A. A. Multifold Emission Enhancement in Nanoimprinted Hybrid Perovskite Metasurfaces. *ACS Photonics* **2017**, *4*, 728−735.

(20) Gao, Y.; Huang, C.; Hao, C.; Sun, S.; Zhang, L.; Zhang, C.; Duan, Z.; Wang, K.; Jin, Z.; Zhang, N.; Kildishev, A. V.; Qiu, C.-W.; Song, Q.; Xiao, S. Lead Halide Perovskite Nanostructures for Dynamic Color Display. *ACS Nano* **2018**, *12*, 8847−8854.

(21) Berestennikov, A. S.; Voroshilov, P. M.; Makarov, S. V.; Kivshar, Y. S. Active Meta-Optics and Nanophotonics with Halide Perovskites. *Appl. Phys. Rev.* **2019**, *6*, 031307.

(22) Tiguntseva, E. Y.; Zograf, G. P.; Komissarenko, F. E.; Zuev, D. A.; Zakhidov, A. A.; Makarov, S. V.; Kivshar, Y. S. Light-Emitting Halide Perovskite Nanoantennas. *Nano Lett.* **2018**, *18*, 1185−1190.

(23) Makarov, S.; Furasova, A.; Tiguntseva, E.; Hemmetter, A.; Berestennikov, A.; Pushkarev, A.; Zakhidov, A.; Kivshar, Y. Halide-Perovskite Resonant Nanophotonics. *Adv. Opt. Mater.* **2019**, *7*, 1800784.

(24) Manjappa, M.; Srivastava, Y. K.; Solanki, A.; Kumar, A.; Sum, T. C.; Singh, R. Hybrid Lead Halide Perovskites for Ultrasensitive

Photoactive Switching in Terahertz Metamaterial Devices. *Adv. Mater.* **2017**, *29*, 1605881.
(25) Chanana, A.; Liu, X.; Zhang, C.; Vardeny, Z. V.; Nahata, A. Ultrafast Frequency-Agile Terahertz Devices Using Methylammonium Lead Halide Perovskites. *Sci. Adv.* **2018**, *4*, eaar7353.
(26) Huang, C.; Zhang, C.; Xiao, S.; Wang, Y.; Fan, Y.; Liu, Y.; Zhang, N.; Qu, G.; Ji, H.; Han, J.; Ge, L.; Kivshar, Y.; Song, Q. Ultrafast Control of Vortex Microlasers. *Science* **2020**, *367*, 1018−1021.
(27) Tiguntseva, E. Y.; Baranov, D. G.; Pushkarev, A. P.; Munkhbat, B.; Komissarenko, F.; Franckevicius, M.; Zakhidov, A. A.; Shegai, T.; Kivshar, Y. S.; Makarov, S. V. Tunable Hybrid Fano Resonances in Halide Perovskite Nanoparticles. *Nano Lett.* **2018**, *18*, 5522−5529.
(28) Shcherbakov, M. R.; Vabishchevich, P. P.; Shorokhov, A. S.; Chong, K. E.; Choi, D.-Y.; Staude, I.; Miroshnichenko, A. E.; Neshev, D. N.; Fedyanin, A. A.; Kivshar, Y. S. Ultrafast All-Optical Switching with Magnetic Resonances in Nonlinear Dielectric Nanostructures. *Nano Lett.* **2015**, *15*, 6985−6990.
(29) Maragkou, M. Ultrafast Responses. *Nat. Mater.* **2015**, *14*, 1086.
(30) Soukoulis, C. M.; Wegener, M. Past Achievements and Future Challenges in the Development of Three-Dimensional Photonic Metamaterials. *Nat. Photonics* **2011**, *5*, 523−530.
(31) Peruch, S.; Neira, A.; Wurtz, G. A.; Wells, B.; Podolskiy, V. A.; Zayats, A. V. Geometry Defines Ultrafast Hot-Carrier Dynamics and Kerr Nonlinearity in Plasmonic Metamaterial Waveguides and Cavities. *Adv. Opt. Mater.* **2017**, *5*, 1700299.
(32) Bennett, B. R.; Soref, R. A.; Del Alamo, J. A. Carrier-Induced Change in Refractive Index of InP, GaAs and InGaAsP. *IEEE J. Quantum Electron.* **1990**, *26*, 113−122.
(33) Burstein, E. Anomalous Optical Absorption Limit in InSb. *Phys. Rev.* **1954**, *93*, 632−633.
(34) Moss, T. The Interpretation of the Properties of Indium Antimonide. *Proc. Phys. Soc., London, Sect. B* **1954**, *67*, 775−782.
(35) Preda, F.; Kumar, V.; Crisafi, F.; Figueroa del Valle, D. G.; Cerullo, G.; Polli, D. Broadband Pump-Probe Spectroscopy at 20-MHz Modulation Frequency. *Opt. Lett.* **2016**, *41*, 2970−2973.
(36) Preda, F.; Oriana, A.; Rehault, J.; Lombardi, L.; Ferrari, A. C.; Cerullo, G.; Polli, D. Linear and Nonlinear Spectroscopy by a Common-Path Birefringent Interferometer. *IEEE J. Sel. Top. Quantum Electron.* **2017**, *23*, 88−96.
(37) Battie, Y.; Resano-Garcia, A.; Chaoui, N.; Zhang, Y.; En Naciri, A. Extended Maxwell-Garnett-Mie Formulation Applied to Size Dispersion of Metallic Nanoparticles Embedded in Host Liquid Matrix. *J. Chem. Phys.* **2014**, *140*, 044705.
(38) Markovich, D. L.; Ginzburg, P.; Samusev, A.; Belov, P. A.; Zayats, A. V. Magnetic Dipole Radiation Tailored by Bubstrates: Numerical Investigation. *Opt. Express* **2014**, *22*, 10693−10702.
(39) Richter, J. M.; Branchi, F.; Valduga de Almeida Camargo, F.; Zhao, B.; Friend, R. H.; Cerullo, G.; Deschler, F. Ultrafast Carrier Thermalization in Lead Iodide Perovskite Probed with Two-Dimensional Electronic Spectroscopy. *Nat. Commun.* **2017**, *8*, 376.
(40) Makarov, S. V.; Zalogina, A. S.; Tajik, M.; Zuev, D. A.; Rybin, M. V.; Kuchmizhak, A. A.; Juodkazis, S.; Kivshar, Y. Light-Induced Tuning and Reconfiguration of Nanophotonic Structures. *Laser Photonics Rev.* **2017**, *11*, 1700108.
(41) Makarov, S.; Kudryashov, S.; Mukhin, I.; Mozharov, A.; Milichko, V.; Krasnok, A.; Belov, P. Tuning of Magnetic Optical Response in a Dielectric Nanoparticle by Ultrafast Photoexcitation of Dense Electron-Hole Plasma. *Nano Lett.* **2015**, *15*, 6187−6192.
(42) Baranov, D. G.; Makarov, S. V.; Milichko, V. A.; Kudryashov, S. I.; Krasnok, A. E.; Belov, P. A. Nonlinear Transient Dynamics of Photoexcited Resonant Silicon Nanostructures. *ACS Photonics* **2016**, *3*, 1546−1551.
(43) Shaltout, A. M.; Lagoudakis, K. G.; van de Groep, J.; Kim, S. J.; Vučković, J.; Shalaev, V. M.; Brongersma, M. L. Spatiotemporal Light Control with Frequency-Gradient Metasurfaces. *Science* **2019**, *365*, 374−377.
(44) Shcherbakov, M. R.; Liu, S.; Zubyuk, V. V.; Vaskin, A.; Vabishchevich, P. P.; Keeler, G.; Pertsch, T.; Dolgova, T. V.; Staude, I.; Brener, I.; Fedyanin, A. A. Ultrafast All-Optical Tuning of Direct-Gap Semiconductor Metasurfaces. *Nat. Commun.* **2017**, *8*, 17.
(45) Polli, D.; Brida, D.; Mukamel, S.; Lanzani, G.; Cerullo, G. Effective Temporal Resolution in Pump-Probe Spectroscopy with Strongly Chirped Pulses. *Phys. Rev. A: At., Mol., Opt. Phys.* **2010**, *82*, 053809.
(46) Bohren, C. F.; Huffman, D. R. *Absorption and Scattering of Light by Small Particles*, 1st ed.; John Wiley & Sons: New York, 1983.

https://dx.doi.org/10.1021/acsnano.0c05710
ACS Nano 2020, 14, 13602−13610